CEAS Aeronautical Journal
https://doi.org/10.1007/s13272-025-00931-1

ORIGINAL PAPER

Jet engine vibration model for estimating pylon–wing interface loads for realistic structural excitation

S. F. Zettel[1] · M. Böswald[1] · R. D. Dewald[1] · R. Winter[1]

Received: 20 January 2025 / Revised: 6 October 2025 / Accepted: 17 November 2025

Abstract
The noise passengers experience in aircraft cabins originates from different sources. One of them is structure-borne noise originating from jet engines. In the case of wing-mounted engines, minor imbalances of rotating engine components can result in a vibration of the wing structure. The wing vibrations are transmitted to the fuselage, potentially giving rise to substantial structure-borne noise. While there are state-of-the-art methods for calculating the acoustic emissions of jet engines during relevant flight conditions, i.e., take-off, cruise and landing, this is not the case for operational vibrations of jet engines. This publication focuses on the development of an engine vibration model on the basis of limited data in the early design phase. The result of the vibration model is a vibration load profile that can be used to excite numerical aircraft models. In combination with the respective jet and fan noise excitation profiles acting on the fuselage, this model will enable future studies to perform holistic assessments of the noise acting inside the cabin. The developed model combines a theoretical approach for the estimation of unbalance forces with measurement data from in-flight experiments with a research aircraft. An exemplary vibration load set for a V2500 engine is calculated and applied to a full aircraft model to show the fuselage response.

Keywords Jet engine · Unbalance · Vibration · Structure-borne noise · Fuselage

1 Introduction

The noise inside aircraft cabins can be attributed to several different sources. In the case of jet engine powered aircraft, Wilby [1] identified the three main sources to be boundary layer noise, engine jet and fan noise, and structure-borne noise. The innumerable vortices of different sizes within the turbulent boundary layer surrounding the aircraft fuselage during flight contribute to broad-band noise. The installed engines and subsystems are additional sources of airborne noise transmitted into the cabin. In particular, the jet and fan noise originate from the engines. Furthermore, engines and other systems also excite the structure in the form of vibrations. In particular, the vibrations originating from the unbalance forces of fast rotating disks can be significant. These vibrations are the main focus of this publication.

To enable a holistic assessment of cabin comfort in terms of acoustics and vibration in the early design stages of an aircraft, it is necessary to describe the noise and vibration sources accurately and cost-effectively, and simple models for physically complex phenomena are quite useful during this stage. With respect to jet engine vibrations, vibration measurements or detailed finite element (FE) models are rarely available at this stage. Therefore, models with the ability to predict the realistic behavior of these sources need to be developed.

This publication focuses on developing a predictive model for jet engine vibrations. This requires the approximation of the maximum permissible unbalance forces of the rotors at their bearing locations. The engine rotation speeds during relevant flight conditions are considered for this purpose. While this approach is theoretical, the model will be improved with realistic assumptions gathered from measurements performed during flights with real aircraft. Furthermore, FE models of relevant aircraft components can be used to further improve model predictions. The goal is to provide relevant vibration loads in the pylon–wing interface of an aircraft. The vibration model is only capable

✉ S. F. Zettel
sebastian.zettel@dlr.de

[1] German Aerospace Center (DLR), Institute of Aeroelasticity, Göttingen, Germany

Published online: 10 December 2025

of estimating the vibrational loads perpendicular to the jet engine shafts resulting from unbalances. Possible vibrations occurring in the thrust direction due to blade–stator interactions or combustion chamber vibrations are not considered. The frequency range of interest for this publication is below 500 Hz. This range is chosen according to the findings of Biermann et al. [2], where experimental structural response data of a laboratory fuselage structure revealed that this frequency range was the frequency range of most structure-borne noise for fuselages of dimensions similar to that of the Airbus A320s.

In Sect. 2 of this publication, the predictive engine vibration model is explained. Section 3 outlines the available experimental data and other information used as model parameters and inputs. In Sect. 4, the setup of the investigated mechanical system is presented, and associated FE models are outlined. In Sect. 5, a set of vibration loads is calculated with the predictive engine-vibration model, and the respective load spectra are discussed. In Sect. 6, the calculated loads are applied to a full aircraft FE model, and the resulting structural response is presented and discussed.

2 Engine vibration model

The core of the engine vibration model is the approximation of unbalance forces acting at the bearing locations inside the engine. The balancing of rotors is a state-of-the-art procedure outlined in engineering standards. Therefore, with a given set of design data for a jet engine, including geometric information (i.e., shaft lengths, bearing and stage locations and the respective masses with the corresponding center of gravities (COGs)), the permissible unbalances can be calculated. Typically, balancing is performed for the maximum rotation speed of a rotor. To calculate the unbalances at relevant operational conditions, the jet engine's rotation speed during a characteristic flight condition, such as a *cruise,* must be known. Furthermore, the vibration spectra of jet engines or machines with rotating components generally exhibit harmonic components.

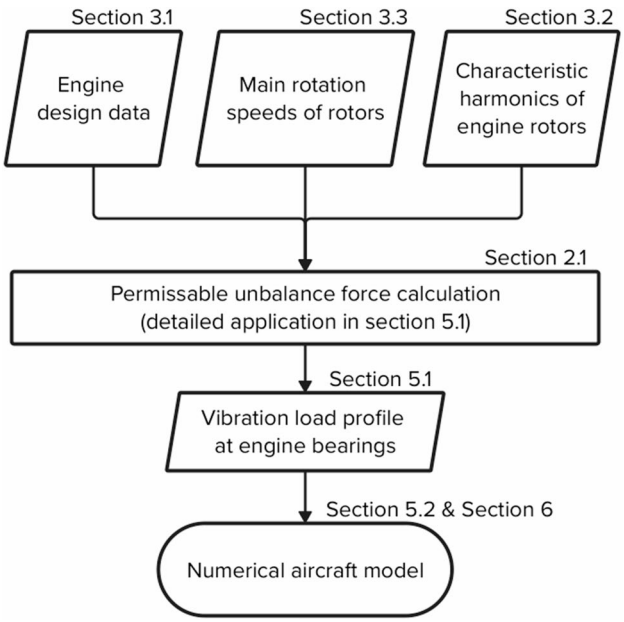

Fig. 1 Engine vibration model process flowchart

The combination of these three crucial pieces of information (i.e., jet engine design data, main rotor speeds and characteristic harmonics) described here enables the calculation of vibratory loads acting at the bearing locations inside the engine. In the current application, the resulting loads can be used to excite numerical aircraft models and study their response. A visual representation of the fundamental approach of the engine vibration model with reference to the respective sections in this study is shown in Fig. 1.

While the calculation of the permissible unbalance forces is a given process described by an engineering standard, the information necessary to calculate a realistic vibration load profile can be acquired only by evaluating experimental data and using given engine design data. Section 2.1 outlines the standardized process of calculating permissible unbalance forces for elastic rotors. The input data necessary to create a realistic model are engine- and operating-point-specific values that will be covered in Sect. 3.

2.1 Unbalance forces under stationary conditions

Balancing is a state-of-the-art procedure for rotating equipment in many industries. This approach ensures permissible vibration forces in the overall system according to the given eccentricity limits of the rotors for the application areas in which the system operates. The engineering standard DIN ISO 1940–Part 1 [4] and its subsequent ISO standards are the basis for the following unbalance force calculation assuming rigid rotors.

The following paragraph is a rephrased summary from Zettel et al. [3]. Regarding the quality G of unbalance forces with unit $[\mathrm{mm \cdot s}]$, the engineering standard requires values below *0.4* $\mathrm{mm \cdot s}$ for rotating drives in high-precision machines and *4000* $\mathrm{mm \cdot s}$ for slow running heavy machinery cranks. For jet engines, the engineering standard recommends an unbalance quality of G=*6.3* $\mathrm{mm \cdot s}$. Using this value, the permissible unbalance U_i of a given rotor can be calculated via

$$\mathrm{U_i} = 1000 \cdot \frac{\mathrm{G} \cdot \mathrm{m_{Rotor}}}{2\pi \cdot \Omega} \cdot \mathrm{k_i} \quad [\mathrm{g \cdot mm}] \tag{1}$$

with the rotor mass m_{Rotor} in [kg] and the maximum rotation speed of the rotor Ω in $\left[\frac{1}{s}\right]$. The permissible unbalance is calculated per existing bearing location in a rotor system.

In simple isostatic cases with two bearings, the load fraction k_i [-] can be calculated via static equilibrium. Complex cases with more than two bearings can be obtained via a numerical simulation (i.e., the finite element method (FEM)). The unbalance force amplitude of interest is calculated by

$$\hat{\mathrm{F}}_{\mathrm{i}} = 10^{-6} \cdot \mathrm{U}_{\mathrm{i}} \cdot (2\pi \cdot \Omega)^2 \quad [\mathrm{N}]. \tag{2}$$

In the engineering standard, the unbalance force amplitude is calculated for the maximum rotation speed of the rotor. However, the rotor can be safely operated at lower rotation speeds. At the respective speeds, the unbalance forces represent the maximum vibration excitation due to permissible unbalance during standard operation of the rotors. The necessary information for unbalance force calculations includes masses and COGs for low-pressure (LP) and high-pressure (HP) shafts and bladed disks (considered rigid bodies). Furthermore, the bearing locations and rotation speeds of the LP and HP shafts are needed. The values for these required model inputs are established in the following section, where a specific engine is considered.

3 Experimental data used to inform the model parameters

This section covers the preparation of the data required as input to the engine vibration model (i.e., engine rotation speeds at the investigated operation point and their respective harmonics). These input values are necessary to calculate the respective unbalance force amplitudes for the engine rotation speeds. Vibrations associated with unbalance forces are typically largest at the frequency of the engine's rotation, but harmonics of this frequency are included in this model to make it more realistic.

The basis for identifying these input values is a set of experimentally acquired data from flight tests with the DLR research aircraft ATRA (Advanced Technology Research Aircraft). The DLR conducted several flights with the ATRA in 2012 within the *Simkab* project. The project focused on vibroacoustic assessment of aircraft cabins [5] via an extensive setup of measurement equipment installed throughout the aircraft. During the flights, microphones and unsteady pressure sensors were installed both inside and outside the fuselage and in the cabin. Accelerometers measure the vibration response of fuselage frames, stringers and crossbeams. The vibrations of the secondary structures, i.e., the floor panels and cabin lining, were also measured. Microphones in the cabin cavity measured the cabin noise. In addition, the relevant parameters regarding the aircraft flight conditions were also recorded from the electronic flight control system. These included time-domain data, tracking of the flight speed, flight altitude, angle of attack and normalized engine shaft rotation speeds.

Table 1 V2500 engine shaft rotation speeds during relevant flight conditions normalized to the maximum speeds of the LP and HP shafts

Flight condition	N1 (LP shaft) (%)	N2 (HP shaft) (%)
Take-off	88	92
Climb	87	88
Cruise	76	83
Descend	30	64

3.1 Operating points of the engine

This subsection is a rephrased summary from Zettel et al. [3]. The rotation speeds of low- and high-pressure shafts of jet engines are highly dependent on flight conditions and atmospheric parameters. Additionally, there is no fixed ratio between the speeds of the two shafts—they rotate independently. For example, during take-off, the ratio of rotation speeds between low- and high-pressure shafts can differ from the ratio between both shafts during cruise flight. Therefore, determining exact rotation speeds for certain flight conditions is not trivial and can ideally be deduced from in-flight data.

The DLR ATRA has two International Aeroengines V2500 jet engines from the manufacturer International Aeroengines. On the basis of the available flight data during the Simkab campaign, it was possible to identify the normalized rotation speeds of the shafts during different flight conditions (see Table 1).

In detail, the time-domain data of normalized engine shaft rotation speeds, flight altitudes and flight speeds were analyzed to identify time intervals describing the four flight conditions (see Table 1) on the basis of their usual flight altitude and speed. For example, take-off is characterized by an increase in flight speed when the altitude only slightly increases, and during cruise, the flight speed and altitude are more or less constant. Accordingly, the average normalized engine shaft rotation speeds for these time intervals were calculated. The values provided in the table above have no general validity for all the engines. These values apply only to the V2500 engine in combination with DLR ATRA. Additionally, the values might change slightly for other flights due to different environmental conditions. However, these are the most-detailed data available to the authors.

3.2 Engine harmonics

Harmonics are additional peaks that appear in a frequency spectrum with an integer multiple (or integer fraction in the case of subharmonics) of the actual rotation speed of

a system. These harmonics appear in the case of a periodic response to harmonic excitation and are thus caused by nonlinear system behavior. In this context, sources of nonlinear behavior can include misalignment, shaft bending, mechanical looseness and bearing effects [6].

The following paragraph is a rephrased summary of Zettel et al. [3]. The measurements from the Simkab flight tests with the DLR ATRA also included accelerometers installed on the fuselage structure. The measured structural response includes excitation from a variety of sources, including the turbulent boundary layer, engines, and other on-board systems. The evaluation of the response data from Norambuena et al. [5] revealed acceleration peaks at the N1 and N2 rotation speeds of the jet engines as well as harmonics, as shown in Fig. 2. The figure shows the autopower spectral densities with a frequency resolution of 1 Hz and decibel intervals of 20 dB on the vertical axis of one acceleration channel for a set of different flight conditions during the Simkab experiments. The color scale (dark blue to yellow) of the individual lines indicates increasing dynamic pressure. The overall fuselage response increases over frequency due to the increasing impact of the turbulent boundary layer, which acts on the fuselage's outer surface, for higher frequencies.

Owing to the different flight conditions, the engine rotation speeds can vary, which was previously mentioned in Sect. 3.1. This is the reason for the frequency variation of certain response peaks. The gray indicator bars center around the calculated rotation speeds for N1 and N2, according to the cruise data in Table 1, as well as the first subharmonic $0.5 \times$N1 and the first higher harmonic $2 \times$N1, with a variance of $\pm$ 5%. The center frequencies for the harmonics were calculated by simply multiplying N1 by factors of 0.5 and 2.

The harmonics show significant peaks in the response spectrum of the fuselage. Therefore, they are incorporated into the engine vibration model. In addition to the actual main rotation frequencies of N1 and N2, the FE model (see Sect. 4) is also excited via the harmonic frequencies. As a result, more-realistic conditions are obtained, as they are present during operation. The first higher harmonic of N2, which is $2 \times$N2, is not present in the fuselage response spectrum, as it is outside the measured frequency band. However, it is included in the model to cover the upper range of the investigated frequency range of up to 500 Hz. Similar to $2 \times$N1, it is assumed that the first higher harmonic of the HP shaft ($2 \times$N2) also has a nonnegligible effect on the engine vibrations.

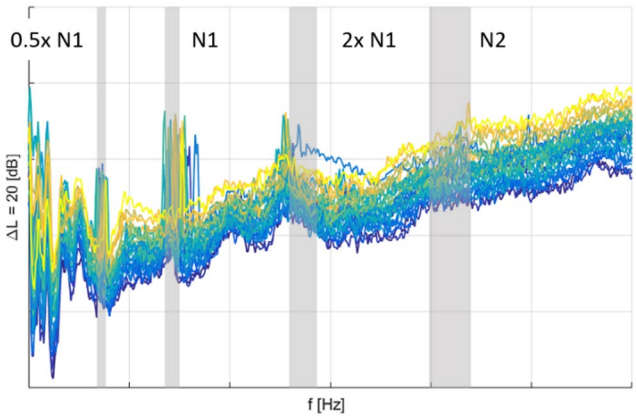

Fig. 2 Autopower spectral densities of an accelerometer under different flight conditions for varying dynamic pressure levels (low: dark-blue; high: yellow) [5] with added indicators for N1 and N2 speeds and their harmonics (each with $\pm$ 5% variance)

Owing to the installation of accelerometers on the fuselage structure, it is not certain if the present harmonic components only arise from the rotor system in the engine. Additionally, joints in the engine–pylon and pylon–wing interfaces, as well as the wing structure itself, might be a source of nonlinearities that result in harmonics. However, the present measurement data are currently the only available source of information regarding harmonic components in the V2500 engine. Acquiring measurement data on or closer to the engine would allow us to gather insights regarding the harmonic components originating exclusively from the jet engine.

While the amplitudes of the unbalance forces at the main rotation speeds of the rotors can be calculated via the approach described in Sect. 2.1, this is not the case for the harmonic components. The rotors do not rotate at the rotation speeds of the harmonic components; therefore, unbalance force amplitudes cannot be calculated. Instead, dimensionless factors (≤ 1) are used to acquire unbalance force amplitudes for the harmonic components. The amplitudes at the main rotation speeds, i.e., N1 and N2, are used as a basis. The spectra in Fig. 2 were used to identify these factors by calculating the decrease in the autopower spectral density (APSD) at $0.5 \times$N1 and $2 \times$N1 in reference to N1 and $2 \times$N2 in reference to N2. Using the decibel formula for power quantities $L_p = 10log_{10}\left(\frac{P}{P_0}\right)$, the factors β can be acquired by

$$\beta = 10^{-\frac{\Delta L_p}{10}} \quad [-]. \tag{3}$$

where ΔL_p is the decrease in the APSD in decibel. The factors for the harmonic components identified in this subsection are stated in Table 2. The peak decreases between N1 and its first subharmonic and the first higher harmonic are approximately 10 dB and 2 dB, respectively, considering the $\pm$5% frequency variance bars. In the case of the first higher harmonic of N2, the same factor as for the first harmonic of N1 is used for two reasons. First, the frequency is not covered by the spectrum in Fig. 2. Additionally, as

Table 2 Harmonic component power factors

Harmonic	0.5 × N1	2 × N1	2 × N2
β[-]	0.1	0.63	0.63

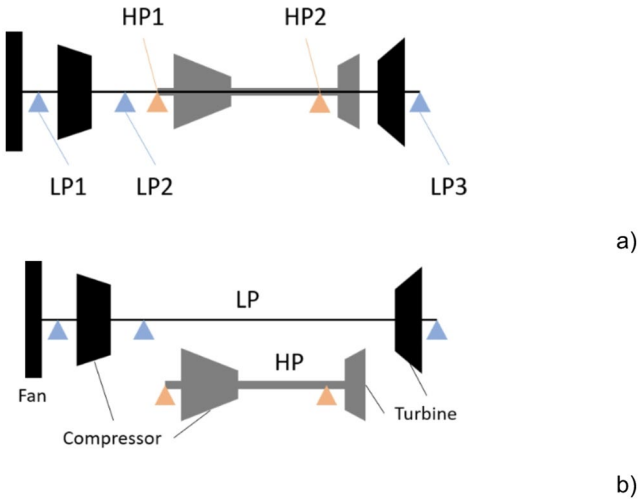

Fig. 3 Schematic representation of the rotor system: **a** complete rotor system, **b** detached rotors; triangles: bearings

stated before, the turbulent boundary layer has an increasing impact on the APSD with increasing frequency across this frequency range; therefore, a clear calculation would not be possible. Accordingly, it is assumed that the power ratio between the unbalance force at N2 and its harmonic has the same ratio as that for N1 and its first harmonic.

3.3 Engine design data

The DLR Institute of Propulsion Technology provided a design data sheet containing all the necessary values regarding the rotor masses and bearing force ratios of a jet engine with specifications similar to those of a V2500. The mentioned design data include information regarding shaft masses, the number of stages per rotor and the masses of disks and blades per disk. To provide easier visualization of the rotor system, an abstract representation is shown in Fig. 3. The coaxial rotor system consists of the LP shaft with its stages and the HP shaft (hollow shaft) with its stages, encasing the LP shaft in the section between the LP compressor and the LP turbine. The LP shaft is supported by three bearings (LP1, LP2 and LP3), and the HP shaft is supported by two bearings (HP1 and HP2).

In Tables 3 and 4, the masses and COG are shown for the low-pressure and high-pressure shafts, respectively.

The component *shaft* describes the rotor shaft without any attached disks or blades. The compressor stages (CSs) and turbine stages (TSs) are indexed with increasing indices from intake to exhaust of the engine. The *fan* plane is set as the reference of the coordinate system utilized for the COG values for both shafts.

Table 3 Low-pressure rotor design data

Component	Mass [kg]	COG [m]
Shaft	58.5	1.42
Fan	143.7	0
CS1	11.3	0.313
CS2	11.8	0.413
CS3	10.5	0.509
CS4	9	0.596
TS1	21.4	2.488
TS2	25.9	2.556
TS3	31.2	2.628
TS4	39.4	2.715
TS5	42.2	2.813
Total	404.9	1.307

Table 4 High-pressure rotor design data

Component	Mass [kg]	COG [m]
Shaft	15.9	1.832
CS1	17	1.047
CS2	13.8	1.183
CS3	11.4	1.278
CS4	9.6	1.353
CS5	8.7	1.414
CS6	6.9	1.464
CS7	10.8	1.509
CS8	9.1	1.547
CS9	7.2	1.581
CS10	6.6	1.609
TS1	58.6	2.253
TS2	70.5	2.349
Total	246.1	1.882

Table 5 Bearing locations of engine shafts and indicators for load carrying capabilities

Bearing	LP1	LP2	LP3	HP1	HP2
Location [m]	0.31	0.88	2.73	0.96	2.02
Function (r,a)	*r & a*	*r*	*r*	*r & a*	*r*

Furthermore, the locations of the bearings are listed in Table 5. The bearing locations are shown in the same coordinate system as the COGs of the rotor components. Additionally, each bearing is tagged according to its load-carrying capabilities, either with r – radial and/or a – axial.

4 Mechanical system setup and FE model

To estimate loads at the interface between the pylon and wing, it is necessary to have a substitute model at hand that represents the mechanical system, including the engine and pylon. A general overview of the full mechanical system, including the wing, pylon and engine, is presented in

Fig. 4a. There are two attachment points between the pylon and the wing as well as between the pylon and the engine (see Fig. 4b). Each attachment point transfers forces in certain degrees of freedom (DOFs), as shown in Fig. 4c and d. The forward attachment points (points to the left in Fig. 4c and d) at both interfaces transmit the thrust in the x-direction and the load resulting from the engine weight as well as possible lateral forces. The aft attachment points also transmit loads arising from the engine weight and lateral forces but do not transmit any force in the x-direction. This permits free thermal expansion of the engine structure in the x-direction. In the engine–pylon interface, the loads acting about the x-axis in the form of a moment are captured at the aft attachment point, whereas in the pylon–wing interface, they are captured at the forward attachment point.

The interface of interest for load estimation is located between the pylon and the wing. To estimate the forces acting at this interface, an FE model needs to be set up that includes the transfer behavior of the structure to obtain realistic interface loads. This model should be the best possible representation of a system consisting of an engine and a pylon. Figure 4a shows a cut of the engine with indicators for the five bearing locations of the V2500 engine. The unbalance forces are applied at the respective points in the FE model, which represent the bearing locations in the real jet engine.

4.1 FE model of the pylon structure

The pylon is a complex mechanical structure that transfers loads from the engine to the wing. In Fig. 5, a pylon of an Airbus A320 that was equipped with V2500 engines is shown. The figure shows the pylon with aerodynamic covers and piping.

An FE model of the load-carrying structure of the pylon was created. A general overview of the pylon FE model is shown in Fig. 6a and b. In Fig. 6c, a half cut of the pylon showing the internal stiffening of the structure highlighted in dark gray is presented. The overall model consists of a box beam meshed with four-node plate elements. The frame structure attached to the front part of the pylon box beam forms the front attachment point to the engine (see Fig. 4b as a reference) and is also modeled with four-node shell elements. The pylon is manufactured from titanium. The material properties, $E_{Ti} = 115MPa$, $\rho_{Ti} = 4500\frac{kg}{m^3}$, and $\nu_{\mathrm{Ti}} = 0.277$, are set appropriately in the FE model. Furthermore, a material damping of $G = 0.02$ is considered. With the chosen mesh density, a frequency range of up to 500 Hz can be evaluated. The upper limit of the frequency range was calculated by performing a wavenumber analysis on the numerical data and adapting the mesh to a density that considers six elements per wavelength. An update of

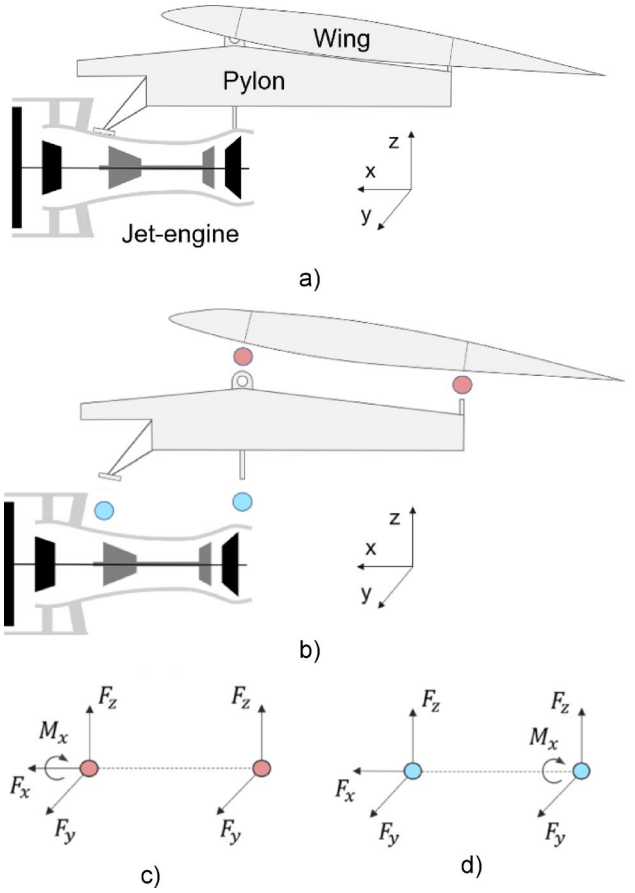

Fig. 4 Mechanical system overview, **a** Illustration of engine, pylon and wing system, **b** Indications for connection points between components, **c** Load transfer DOF for pylon-wing interface [3], **d** Load transfer DOF for pylon-engine interface [3]

Fig. 5 Side view of a pylon of an A320 aircraft during a modal test

the FE model with the available measurement data of the pylon was only possible to a limited extent. The measured pylon structure contains a large amount of added mass due to the unspecified attachments in the form of pipes, covers and fasteners. A detailed FE model is still in development. Therefore, the current FE model is the best the authors are able to use at the moment.

A detailed FE model of a V2500 engine was not available. Therefore, the engine structure was assumed to be rigid and represented via beam elements (CBEAMs), which connect the bearing locations with the pylon–engine interfaces. The use of rigid-body elements (RBE) was not feasible because of the setup of the model. In the case of RBE2

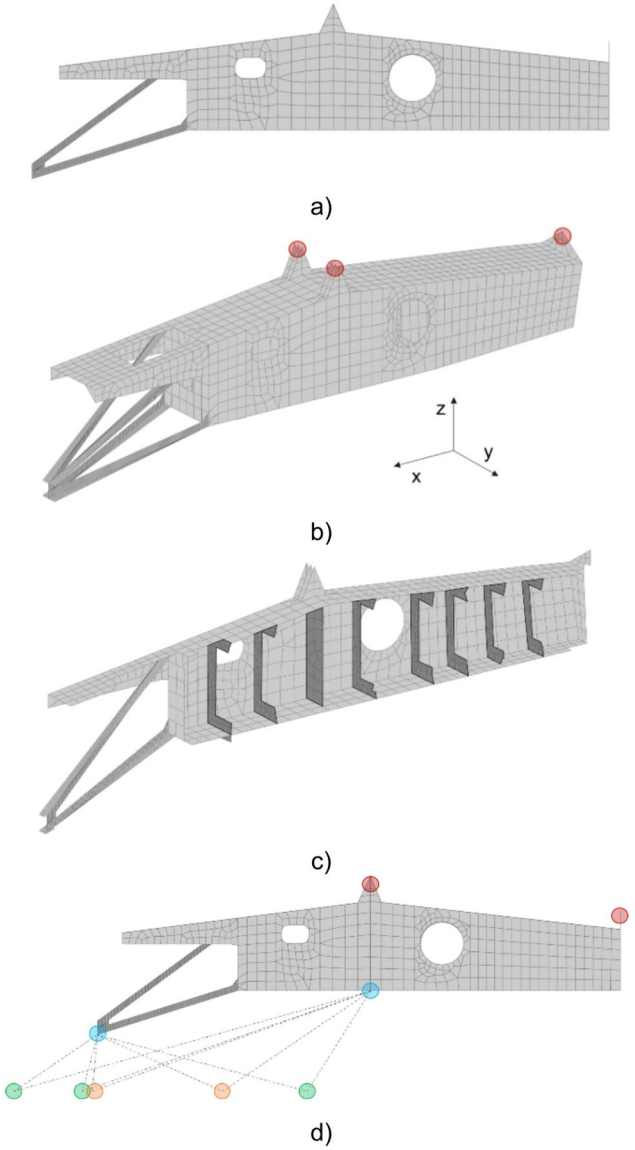

Fig. 6 Pylon model overview: **a** Side view, **b** Iso view, **c** Iso with centric cut and frame highlights, **d** Pylon with RBE connections (green: LP bearings, orange: HP bearings)

(Nastran-specific nomenclature), the chosen dependent nodes, the three points at the engine–pylon interface, cannot be present in more than one RBE2 at the same time. Figure 6d shows a visualization of the beam connections that represent the substitute engine structure. Locations in which the lines between bearings and attachment points cross each other are not connected but rather move freely. The relative distances between the engine's bearing locations and the pylon's engine attachment points are derived from the figures provided in [7] and are considered to be reasonably accurate. Having correct distances between bearing points and attachment locations is important for generating valid moments at the attachments from the translatory excitation forces acting on the bearings. The green and orange indicators represent the locations of the LP and HP shaft bearings in the engine–pylon interface (see blue markers in Fig. 4b) as a reference), respectively.

The beam connections were set up with rods having a circular cross-section with a radius of $r = 0.01\ m$, a Young's modulus with a factor of 1000 greater than the pylon's modulus and a density of $\rho = 0.1 \frac{kg}{m^3}$. A high Young's modulus is chosen so that the engine substitute structure does not have a superposed impact on the response of the pylon structure up to 500 Hz. The density is set to a low value, as the masses of the engine casing and the rotors are represented by point masses at the bearing locations.

The point masses are a combination of rotor masses and the mass of the engine casing. The individual point masses are calculated via fractional weights, which are derived from rotor masses with the respective load fractions k, and the average engine casing mass per bearing. As there is no detailed information on the engine casing's mass distribution along the engine length, every bearing location is assumed to be assigned an average fractional mass of the casing. The following equations, according to Zettel et al. [3], represent the individual point masses at the bearing location i:

$$\mathrm{m_{LP\,bearing,i}} = \mathrm{m_{LP\,rotor}} \cdot \mathrm{k_{LP,i}} \quad [\mathrm{kg}], \tag{4}$$

$$\mathrm{m_{HP\ bearing,i}} = \mathrm{m_{HP\ rotor}} \cdot \mathrm{k_{HP,i}} \quad [\mathrm{kg}], \tag{5}$$

$$\overline{\mathrm{m}}_{\mathrm{casing}} = \frac{\mathrm{m_{engine}} - \mathrm{m_{LP\ rotor}} - \mathrm{m_{HP\ rotor}}}{\mathrm{n_{bearing}}} \quad [\mathrm{kg}], \tag{6}$$

$$\mathrm{m_{LP\ bearing\ total,i}} = \mathrm{m_{LP\ bearing,i}} + \overline{\mathrm{m}}_{\mathrm{casing}} \quad [\mathrm{kg}], \tag{7}$$

$$\mathrm{m_{HP\ bearing\ total,i}} = \mathrm{m_{HP\ bearing,i}} + \overline{\mathrm{m}}_{\mathrm{casing}} \quad [\mathrm{kg}]. \tag{8}$$

Each bearing location is connected to the front and rear attachment points of the pylon. For the substitute model of the engine structure, no RBEs are used, and the connection between the forward attachment point of the engine and the pylon is modeled via RBE2s. The engine structure connections (ESCs) starting from the bearings and ending at the attachment points of the pylon converge at one point close to the respective attachment points. The aft attachment point is just a single point, and the convergence point of the ESCs is connected point-to-point via an RBE2. The nose on the pylon is the dependent node. In the case of forward attachment, the respective convergence point of the ESCs cannot be connected to the attachment location directly, as the forward attachment of the pylon consists of a double-T section; see the end of the forward pylon attachment in Fig. 4b as a reference. The double-T section consists of 33 nodes.

Therefore, the convergence point of the ESCs is attached to the forward attachment double-T section of the pylon via RBE2s, whereas the nodes of the attachment plate act as the dependent nodes. For both RBE2 connections, i.e., forward and aft connections, the DOFs for load transfer are set according to the transmitted forces and moments; see Fig. 4d as a reference.

4.2 Simulation setup

The excitation of the model is performed with discrete forces acting on each bearing location. An excitation in the form of an unbalance force is a circulatory force acting in the radial direction of the bearing and can be represented by a combination of two orthogonal forces with a phase shift of $\frac{\pi}{2}$ acting in the y–z-plane; see Fig. 6b as a reference. As there is not only one rotation speed exciting the structure but also at least two, one for the LP rotor and HP rotor each, and additionally possible harmonics, the force combinations need to be set accordingly

$$\mathrm{F_{i\Omega,y}}\left(\mathrm{t}\right) = \hat{\mathrm{F}}_{\mathrm{i}}\left(\Omega\right) \cdot \mathrm{e}^{\mathrm{j}\left(2\pi\cdot\Omega\cdot\mathrm{t}+\theta_{\mathrm{i}}\right)} \quad [\mathrm{N}], \tag{9}$$

$$\mathrm{F_{i\Omega,z}}\left(\mathrm{t}\right) = \hat{\mathrm{F}}_{\mathrm{i}}\left(\Omega\right) \cdot \mathrm{e}^{\mathrm{j}\left(2\pi\cdot\Omega\cdot\mathrm{t}+\theta_{\mathrm{i}}-\frac{\pi}{2}\right)} \quad [\mathrm{N}], \tag{10}$$

where $\boldsymbol{i}$ represents the bearing location and where $\boldsymbol{j}$ is a complex number. The parameter $\boldsymbol{\theta}$ enables the inclusion of an additional phase shift between the forces at the different bearing locations for a specific excitation frequency. In the time-domain, a combination of forces for all considered rotation speeds results in an excitation signal that contains phase relationships between the frequency-dependent forces at their bearing locations. However, considering a set of forces at only one specific frequency, the forces would all be in-phase for the case where $\boldsymbol{\theta_i} = 0$. While this is an idealistic case for the excitation of the system, no reference has been found indicating which level phase differences occur in unbalances on one rotor. Accordingly, this publication considers only in-phase excitations for the respective excitation frequencies $\boldsymbol{\Omega}$. A simple approach to tune the phases for a more realistic excitation could be to use random values for the phases. The authors assume this to be a reasonable approximation of the real excitation without performing a detailed study.

The simulation is performed as a direct frequency response simulation in Nastran with solution SOL 108. For each discrete frequency, the respective forces are applied to the model at the bearing locations. The simulation results in one set of reaction forces at the attachment points; see the red indicators in Fig. 6d as a reference. For the forward attachment points, the reaction forces exist for the x-, y- and z-directions and for the aft attachment point in the y- and z-directions. These directions are in accordance with the fixed degrees of freedom in Fig. 4c and d.

Table 6 Generic engine rotation speeds

Description	0.5×N1	N1	2×N1	N2	2×N2
Frequency [Hz]	35	70	140	200	400

5 Calculation of the interface loads

To calculate the interface loads between the pylon and wing, it is necessary to calculate the unbalance forces acting on the jet engine and apply these forces to the FE model presented in Sect. 4.1 (see flowchart in Fig. 1 as a reference). In Sect. 2.1, the process of the unbalance calculation is described, and in Sect. 3, all the necessary supplementary information for the calculation is presented. The only missing values to calculate the interface loads are the main jet engine rotations for the N1 and N2 shafts, the load fractions for the rotor systems bearings and the substitute masses of the engine, which need to be assigned to the bearing locations in the FE model. This section covers the calculation of the missing values, and the resulting load set acting at the bearing locations is presented. Furthermore, the calculated load set is applied to the FEM model, and the resulting pylon–wing interface loads are presented and discussed.

5.1 Calculation of unbalance load set

First, the main rotation frequencies for the unbalance load set are chosen, and the respective harmonics are calculated. Aircraft spend the longest amount of time in cruise flight conditions, which describes the stationary flight speed at a given altitude. Therefore, considering passenger comfort during this flight condition is highly important. The percentage values for *cruising* are used and applied to the maximum rotation speeds of the N1 and N2 shafts for the V2500 engine. The resulting rotation speeds for N1 and N2 during cruise were slightly altered because of nondisclosure. Accordingly, the frequencies for 0.5×N1, 2×N1 and 2×N2 can be calculated with the respective integer factors. The full set of frequencies used for further calculations are presented in Table 6.

For the calculation of the missing load fractions, the geometrical and mass information in Table 3 through Table 5 are used. In accordance with the balancing standard [4], the load fractions for a rotor with two bearings can easily be calculated by moment equilibrium. In the case of the HP rotor, the calculation for the load fractions is performed by a moment equilibrium about the HP1 bearing

$$\mathrm{m_{HP\ Rotor}} \cdot \mathrm{g} \cdot \left(\mathrm{l_{HP\ COG}} - \mathrm{l_{HP1}}\right) = \mathrm{F_{HP2}} \cdot \left(\mathrm{l_{HP2}} - \mathrm{l_{HP1}}\right) \tag{11}$$

where g $\left[\frac{m}{s^2}\right]$ is the gravitational constant, l is the distance in [m] and F is the reaction force in [N] of the respective bearing. Finally, the load fractions can be calculated with

$$\mathrm{k_{HP2}} = \frac{\mathrm{F_{HP2}}}{\mathrm{m_{HP\ Rotor}} \cdot \mathrm{g}} \quad [-] \tag{12}$$

$$\mathrm{k_{HP1}} = 1 - \mathrm{k_{HP2}} \quad [-] \tag{13}$$

The load fractions result in $k_{HP1} = 0.13$ and $k_{HP2} = 0.87$.

For the LP rotor, a simple approach with a moment equilibrium is not possible, as the system is overdetermined. Therefore, a simple FE model consisting of a beam, representing the shaft, with the respective masses modeled as point masses and constraints at the bearing locations, was set up. The constraints are set according to the load-carrying properties of the bearings, which are outlined in Table 5. The shaft was modeled as an elastic beam with a circular cross section and a diameter of $d_{LPshaft} = 0.06m$. The material properties were set to steel properties (medium-carbon low-alloy steel according to [8]) commonly used for shafts in jet engines ($E = 200MPa$, $\rho = 7850\frac{kg}{m^3}$ and $\nu = 0.29$).The model was used in a linear static analysis with a gravitational load of g = 9.81 $\frac{m}{s^2}$. The load fractions result in $k_{LP1} = 0.47$, $k_{LP2} = 0.09$ and $k_{LP3} = 0.44$.

The calculated load fractions k and the rotor masses stated in Tables 3 and 4 are combined. The substitute point masses of the engine can be calculated via Eq. (4) through Eq. (8). The provided data sheet for the engine does not provide information regarding the total engine mass. However, the engine maintenance webpage of the MTU [9] states that the engine mass is $m_{engine} = 2480kg$. Accordingly, all engine substitute masses are calculated and are presented in Table 7

The resulting maximum permissible unbalance forces via the process described in Sect. 2.1 using the harmonic power factors (see Table 2) are presented in Table 8.

The force values in the N1 and N2 columns were multiplied by the dimensionless harmonic power factors to acquire the respective forces for the harmonic components. These force amplitudes are used to set up the excitations according to Eq. (9) and Eq. (10) for the direct frequency response simulation in NASTRAN with the FEM model described in Sect. 4.1. The resulting interface loads are covered in the following subsection.

5.2 Pylon–wing interface load spectrum

The spectra in Fig. 7 show the respective amplitudes of the loads at the pylon–wing attachment points of the model at single discrete frequencies, i.e., 0.5 × N1, N1, 2 × N1, N2, and 2 × N2. Each amplitude level was acquired by performing an individual simulation with the FE at the respective frequency. In Figure 7a, the loads for the aft attachment point are zero, as this point only transfers loads in the y- and z-directions. The loads at N1 are high in comparison to the loads at the other frequencies. The reason for the high loads at N1 is the local response peak of the FE model close to N1, which is shown in Fig. 8. The spectrum represents the spatially averaged frequency–response function over all computational nodes within the FE model of the pylon. A generic excitation in the x-direction with a unit force acting on all the LP shaft bearing locations was used. The gray lines indicate the engine rotation speeds 0.5 × N1, N1 and 2 × N1. The line at N1 (second gray line) is close to a local response peak.

Table 7 Point masses assigned to bearing locations in the FE model representing the condensed engine mass

Bearing	LP1	LP2	LP3	HP1	HP2
Mass [kg]	556.1	402.2	544	397.8	579.9

Table 8 Unbalance forces at engine bearings for all considered engine rotation speeds

Frequency	0.5×N1	N1	2×N1	N2	2×N2
LP1 [N]	53	531	334	–	–
LP2 [N]	9	93	59	–	–
LP3 [N]	50	496	312	–	–
HP1 [N]	–	–	–	259	163
HP2 [N]	–	–	–	1689	1064

An inspection of the respective operational deflection shape at N1 shows that the FE model sways back and forth in the x-direction. The reason is that even though the FE model is only excited in the y- and z-directions, there is a resulting force in the x-direction due to the structural setup of the engine substitute model. Therefore, the model performs swaying deflection in the x-direction, and the corresponding reaction forces result at the forward attachment points, which constrain the model in the x-direction. The missing constraint in the x-direction at the aft attachment point, as explained in section 4, is the reason that the full load in the x-direction is captured by the forward attachment points. This results in a higher load at these points. In the introduction, it was stated that no x-direction forces in the form of an excitation at the bearing location would be included. This is only meant for purposely applied x-direction forces in the form of an excitation at the bearing locations but not the resulting x-direction forces discussed here. Furthermore, the resulting forces in the x-direction at the forward attachment points in the pylon-wing interface, shown in Fig. 4b, are dependent on the number of *dependent nodes* chosen for the RBE2 connection.

The loads in the y-direction are presented in Fig. 7b. In general, the loads in the y-direction are smaller than the

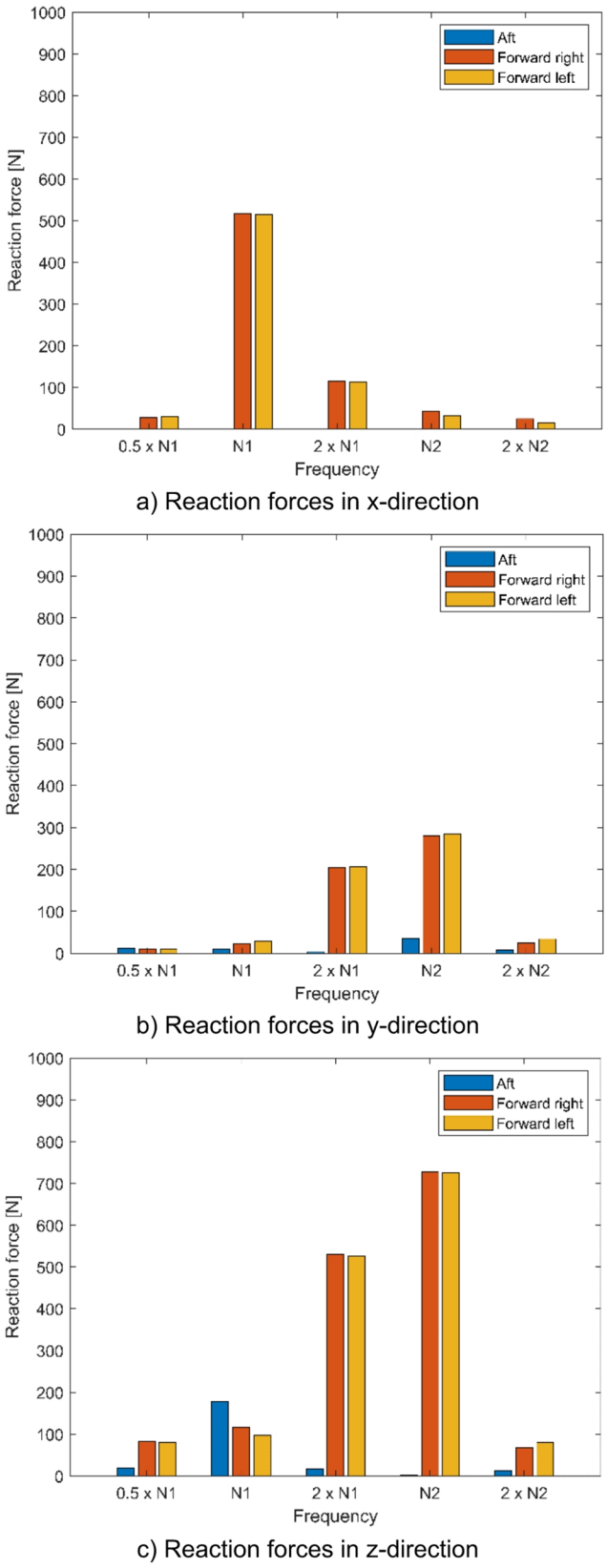

Fig. 7 Amplitude spectra of the reaction forces at the pylon–wing attachment points in the **a** x-, **b** y- and **c** z-directions

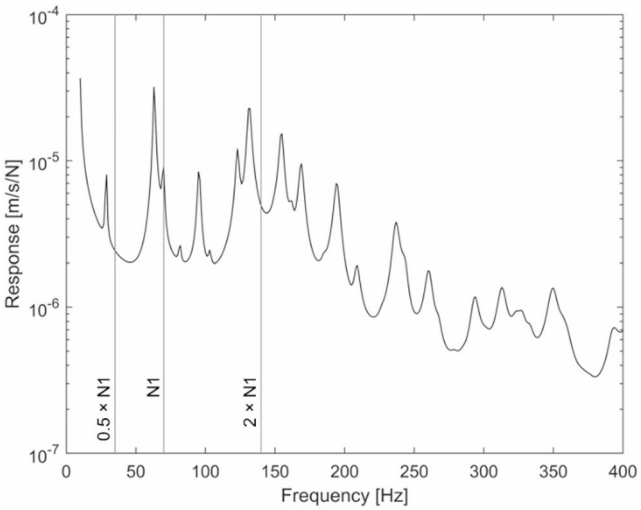

Fig. 8 Summarized frequency response of pylon-related FE model nodes due to generic unit force excitation at the LP bearing locations; dashed lines: engine rotation speed of the LP shaft

loads in the z-direction (see Fig. 7c). The forward attachment points capture only the reaction forces in the y-direction resulting from the excitation forces on the bearings in the same direction. However, the y-direction forces in the bearings also introduce a moment about the x-axis of the model, which results in additional overlaying forces at the forward attachment points in the z-direction. Therefore, the reaction forces in the z-direction are generally greater than the y-direction reaction forces.

The bar graphs in Fig. 7 only show the amplitudes of the loads. However, the calculated interface loads are complex values that also include information about the relative phase of these loads. The full interface load dataset generated with the presented FE model is shown in Table 9.

6 Structural response of an aircraft fuselage due to engine vibrations

In this section, the pylon–wing interface loads calculated with the approach described in the previous sections are applied to a model of a full aircraft. The FE model is built on the basis of a CPACS (data definition for the air transportation system developed via DLR) dataset via the DLR model generator ModGen. The model consists of approximately $1.67 \cdot 10^6$ nodes and therefore has roughly 10^7 degrees of freedom. The mesh density is adjusted to allow response analysis up to a frequency of 500 Hz. The model is described in detail in the publication of Dewald et al. [10]. The loads are applied to the respective pylon attachment points on the wing box. Additionally, the resulting x-direction loads from the engine vibration model are included in the following aircraft model excitation.

Table 9 Amplitude and phase values for loads at pylon-wing attachment points: a) forward left, b) forward right, c) aft

Frequency		0.5 × N1	N1	2 × N1	N2	2 × N2
a)						
X	$\widehat{F}$[N]	30.1	514.9	112.2	32.3	14.9
	θ[°]	75.9	272.8	263.8	325.8	118.3
Y	$\widehat{F}$[N]	9.5	29.4	205.8	284.1	34.2
	θ[°]	40.3	42.3	80.3	276.5	251.6
Z	$\widehat{F}$[N]	80	96.9	525.9	725.9	80.6
	θ[°]	172.7	145.9	83.7	270.4	254.2
b)						
X	$\widehat{F}$[N]	28.4	517.4	114.7	43.5	24.6
	θ[°]	104	275.6	272.1	205.3	141.4
Y	$\widehat{F}$[N]	9.2	23.4	205.2	280.6	23.9
	θ[°]	321.8	304.7	264.8	89.5	92.2
Z	$\widehat{F}$[N]	81.8	117.1	530.8	727	68.3
	θ[°]	12.8	30	81.4	275.8	265.5
c)						
X	$\widehat{F}$[N]	0	0	0	0	0
	θ[°]	0	0	0	0	0
Y	$\widehat{F}$[N]	11.4	9.2	2.5	34.9	7.6
	θ[°]	3.9	359.5	2.5	359	161.3
Z	$\widehat{F}$[N]	19.5	178.1	16.5	1.3	12.4
	θ[°]	90.2	274.5	268.4	122.8	240.5

In Fig. 9, the structural responses of the aircraft model are shown for the respective frequencies used for the engine vibration model. The subplots show only the response of the cabin structure. The wing responses are not shown here for the sake of simpler interpretation of the results. All the responses are presented with a color scale indicating the normalized velocity response, meaning that all the velocities at a frequency are referenced to the maximum velocity present at this frequency. The respective maximum velocity response is provided in the subplot captions for a general comparison of the present amplitudes. The following analysis aims by no means to provide an exhaustive evaluation of the FE model of the full aircraft (primary structure excluding the engine vibration FE model). Model development has finished just recently. Therefore, no comprehensive evaluation can be provided thus far. The following evaluation provides a short overview of the emerging structural responses due to engine vibrations. A detailed comparison of the respective responses arising from other excitation sources, such as jet and fan noise, is not conducted. Additionally, an evaluation of the potential noise emission into the cabin due to the structural response is not performed.

In Fig. 9a, the response for the first subharmonic of N1 shows a global characteristic. The spatial distribution of the response amplitudes shows some ovalizing shell mode of the fuselage with four structural waves in the circumferential direction and two structural waves in the longitudinal direction. Considering that high-velocity response regions are potential noise-emission areas, the fuselage section in front of the wings and the section at the back of the fuselage may be noisier than the other sections at this frequency. The structural response in Fig. 9b shows a similar distribution to that for the first subharmonic but with shorter wavelengths, which results in a more local response. Figure 9c shows that local effects start to emerge as the region around the wing attachment shows a significant response according to the normalized color scale. In Fig. 9d and e, the responses for the engine frequency and its first higher harmonic are presented. The responses of the fuselage start to show a statistical distribution of the response, as the response of the fuselage is dominated by a multitude of individual skin fields. The statistical distribution implies that the upper frequency limit of the mid-frequency range is exceeded. This region of higher relative frequencies is characterized by wavelengths smaller than the individual components of the structure. Therefore, the overall structural response no longer shows any global deformation, and the response behaves similarly to a statistical distribution of energy. The

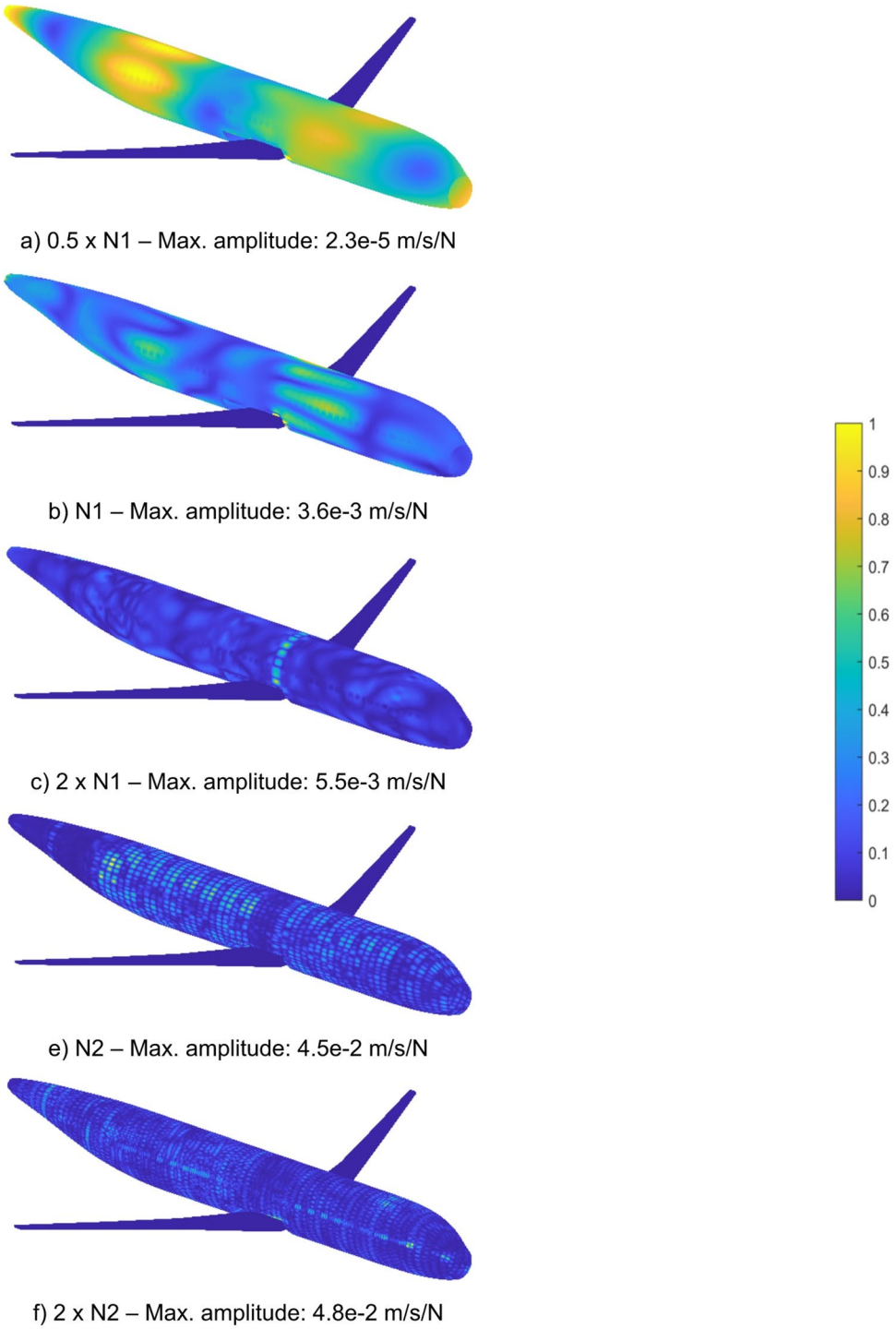

Fig. 9 Fuselage response of the full aircraft model excited with estimated engine vibration forces; color scale: normalized velocity (normalization reference: maximum velocity at every frequency)

term 'skin field' refers to the exterior panels or surfaces of the aircraft that span the underlying frame structure.

The calculated engine vibrations significantly excite the fuselage structure and introduce local effects in different regions. As previously mentioned, investigating only the fuselage vibration responses with respect to engine vibration excitation is not sufficient for performing comprehensive analyses of the noise inside a cabin. Additionally, the impacts of jet noise and fan noise originating from the engines need to be included in the analysis to compare the sources and their impacts on the resulting noise in the cabin. With respect to the full aircraft model used in this study, preliminary results of the aircraft's response to jet- and fan-noise were investigated in the publication of Dewald et al. [10].

7 Conclusion

This publication covered the development of an engine vibration model on the basis of limited data in the early design phase. The model assumes that jet engines have permissible unbalances that induce forces in the bearings that support the rotating assemblies. These unbalance forces can be estimated with an engineering standard. Applying the resulting forces onto a substitute model of the engine–pylon-system enables the estimation of loads at the pylon–wing interface. During development, the engine rotation speeds for low- and high-pressure shafts were identified from in-flight measurement data. Additionally, flight data revealed that the engine harmonics of both shafts contributed substantially to the vibrations of the fuselage. For this reason, the forces on the aircraft due to unbalance forces at the subharmonics and harmonics of the shaft frequencies were considered. The resulting load spectra and phase information for the loads acting at the pylon–wing interface are presented and discussed.

Furthermore, the calculated interface loads are applied to a full aircraft model representing the primary load-carrying structure. The results of the fuselage response for all relevant engine frequencies are shown and discussed. The fuselage shows varying local responses according to the different frequencies.

Overall, the development of the presented model provides one the chance to calculate a set of loads acting in the pylon–wing interface. Accordingly, realistic wing excitations from jet engine unbalance forces can be included in cabin-comfort assessments. To date, the engine vibration model has not yet been validated. The accuracy of the calculated interface loads could be quantified only by a comparison with the respective blocked-force measurements on a similar system setup. A blocked-force characterization provides a full description of the invariant forces of a source, such as an aircraft engine in this case. This full description provides a set of force spectra for different operational conditions of an engine that can be directly compared with the force spectra of the engine model. A detailed description of the application of the blocked forces method can be found in [11] and, lately, in the ISO 20270 standard “Indirect measurement of blocked forces” [13].

Furthermore, while every effort has been made to create a vibration model that is as realistic as possible, no detailed engine casing FE model has been included. The inclusion of a detailed model of the engine casing increases the model’s accuracy for the following reasons. A realistic representation of the stiffness and mass distribution results in the formation of realistic structural wave patterns in the engine casing structure. These factors affect the resulting vibrational loads at the engine–pylon interface and, accordingly, the subsequent loads at the pylon–wing interface. The current engine substitute model can be seen as close to ideally stiff compared with the rest of the model’s structure. Additionally, while the mass of the engine is close to reality, condensation into one point does not account for the real moments of inertia of an actual engine casing structure. In conclusion, the substitute model of the engine structure simply cannot account for dynamic effects as a detailed engine casing model would.

With respect to the applicability of the presented model, the following conclusions can be drawn. The fundamental approach of using the balancing standard is generally applicable for rotating machinery and easy to use. Therefore, this approach is not limited to jet engines. However, regardless of the type of rotating machinery under investigation, it is crucial to have additional measurement data or detailed approximations from other dedicated models at hand, e.g., system design data, main rotation speeds and harmonics. Furthermore, assuming a rigid rotor is a conservative approach. Improvements are possible by assuming an elastic rotor in cases of detailed information regarding the rotor geometry and materials. The same is true for FE models of relevant structural components of the machinery setup. Without this additional information, the model could not be expected to yield representative data. The simulation setup using direct frequency response analysis and the realization of excitation explained in Sect. 4.2 is generally applicable for rotating machinery when stationary conditions are present. The harmonic components of the model were identified via structural response data acquired on the fuselage structure during flights. More detailed information regarding exact harmonics frequencies could be obtained by measuring jet engine vibrations closer to the actual engine. This approach would also help quantify the harmonic power factors more precisely.

An improvement using an elastic rotor assumption is possible for the following reasons. Assuming a rigid rotor, the rotor does not experience deflections of the shaft center from the axial rotation center. Therefore, this approach results in unbalance forces with positive linear scaling over the rotation speed. The more realistic approach is to assume an elastic rotor. This allows deformations of the rotor and effects such as self-centering at overcritical rotation speeds to be included. The critical rotation speed here refers to the first elastic bending eigenfrequency of the rotor. Near the critical rotation speed, the unbalance forces can be significant. However, aero engines are designed not to operate at critical rotation speeds. Well above the critical rotation speed, the unbalance forces decrease because of the self-centering of the elastic rotor. Using unbalance forces of elastic rotors was not feasible in this publication because information regarding the rotor geometry and materials

was missing. The results acquired with elastic rotor modeling would have been speculative. Therefore, the authors decided to use the conservative approach of the rigid rotor.

Finally, the results of the model are not limited to the application of numerical models. They can also be applied in laboratory experiments to provide realistic excitation conditions. The first application was performed by Norambuena et al. [12], who utilized a controlled shaker setup to excite an Airbus A320 wing in a laboratory setup to perform vibroacoustic characterization.

Author contributions M.B. and R.W. supported in the development of the vibration model and revised the manuscript critically for important intellectual content. R.D.D. prepared the finite element models.

Funding Open Access funding enabled and organized by Projekt DEAL.

Data availability No datasets were generated or analysed during the current study.

Declarations

Conflict of interest The authors declare no competing interests.

References

1. Wilby, J.F.: Aircraft interior noise. J. Sound Vib. (1996). https://doi.org/10.1006/jsvi.1996.0078
2. Biedermann, J., Winter, R., Norambuena, M., Böswald, M.: Classification of the mid-frequency range based on spatial Fourier decomposition of operational deflection shapes. International Congress on Sound and Vibration, London (2017)
3. Zettel, S. F., Böswald, M., Winter, R.: Jet engine vibration model for the estimation of pylon-wing interface loads. DAGA 49, Hamburg, 628–631 (2023).
4. DIN ISO, Mechanical vibration—Balance quality requirements for rotors in a constant (rigid) state—Part 1: Specification and verification of balance tolerances. 1940–1 (2003)
5. Norambuena, M., Böswald, M., Govers, Y.: Vibro-acoustic analysis of flight test data comprising fuselage vibrations, external pressure and interior cabin noise measurements. 54th AIAA Aerospace Sciences Meeting, San Diego (2016). https://doi.org/10.2514/6.2016-1013. Copyright © 2016 by German Aerospace Center (DLR).
6. Scheffer, C., Girdhar, P.: Machinery fault diagnosis using vibration analysis. In: Scheffer, C., Girdhar, P. Practical Machinery Vibration Analysis and Predictive Maintenance, Chapter 5. Newnes (2014). ISBN: 978–0–75066–275–8.
7. IAE V2500 General Familiarisation. IAE International Aero Engines AG (2000).
8. Mouritz, A.P.: Introduction to Aerospace Materials. Woodhead Publishing, AIAA Education (2012)
9. V2500 - MTU Aero Engines. (n.d.). https://www.mtu.de/engines/commercial-aircraft-engines/narrowbody-and-regional-jets/v2500/
10. Dewald, R.D., Klimmek, T., Winter, R.: Parametrische Modellierung der Primärstruktur für die Analyse von Flugzeuginnenlärm. Deutscher Luft- und Raumfahrt Kongress, Hamburg (2024). https://doi.org/10.1007/s13272-025-00888-1
11. Moorhouse, A.T., Elliott, A.S., Evans, T.A.: In situ measurement of the blocked force of structure-borne sound sources. J. Sound Vib. (2009). https://doi.org/10.1016/j.jsv.2009.04.035
12. Norambuena, M.G, Zettel, S.F., Dewald, R.D., Winter, R.: Experimental vibroacoustic characterization of an A320 Wing utilizing a controlled shaker system for artificial engine-vibration excitation. Numerical Methods and Experimental Means for the Integration of Future Propulsion Systems - A Resumé of the Achievements Made within the CleanSky 2 XDC Demonstrator, Springer Nature Switzerland AG (2025).
13. ISO 20270:2019, Acoustics—Characterization of sources of structure-borne sound and vibration - Indirect measurement of blocked forces.